InGaAsP Annular Bragg Lasers: Theory, Applications, and Modal Properties

Jacob Scheuer, *Member, IEEE*, William M. J. Green, *Student Member, IEEE*, Guy A. DeRose, and Amnon Yariv, *Life Fellow, IEEE*

***Abstract*—A novel class of circular resonators, based on a radial defect surrounded by Bragg reflectors, is studied in detail. Simple rules for the design and analysis of such structures are derived using a transfer matrix formalism. Unlike conventional ring resonators, annular Bragg resonators (ABR) are not limited by the total internal reflection condition and can exhibit both large free spectral ranges and low bend losses. The Bragg reflection mechanism enables the confinement of light within a defect consisting of a low refractive index medium (such as air). Strong atom–photon interaction can be achieved in such a structure, making it a promising candidate for sensing and cavity quantum electrodynamics applications. For sensing applications, we show that the ABR structure can possess significantly higher sensitivity when compared to a conventional ring resonator sensor. Lasing action and low threshold levels are demonstrated in ABR lasers at telecommunication wavelengths under pulsed optical pumping at room temperatures. The impact of the intensity and dimensions of the pump spot on the emitted spectrum is studied in detail.**

***Index Terms*—Bragg resonators, integrated optics, photonic crystals, semiconductor lasers.**

I. Introduction

THE PAST FEW years have witnessed a significant increase in research involving circular optical resonators. Resonators are key elements for various applications such as optical communication systems [1]–[6] and biochemical sensing [7], [8], as well as for basic research such as single molecule spectroscopy [9] and cavity quantum electrodynamics (QED) [10], [11] with possible applications in quantum information technologies.

For many of these applications, resonators that exhibit low losses (high Q factor) are required. Particularly for sensing applications and for cavity QED, it is also often desired that the resonators have a small modal volume. These characteristics are required in order to attain strong atom–photon interaction and to probe as small a modal volume as possible. For telecommunication applications, a large free spectral range (FSR) is often desired, which requires the resonators to be of small dimensions.

Manuscript received July 15, 2004; revised January 24, 2005. This work was supported in part by the National Science Foundation under Grant ECS-0401397, in part by the Defense Advanced Research Projects Agency (DARPA) under Grant MDA972-00-1-0022, and in part by the Air Force Office of Scientific Research (AFOSR) under Grant FA9550-04-1-0016.

The authors are with the Departments of Applied Physics and Electrical Engineering, California Institute of Technology, Pasadena, CA 91125 USA (e-mail: koby@caltech.edu).

Digital Object Identifier 10.1109/JSTQE.2005.845614

Circular resonators based on total internal reflection (TIR) that exhibit the combination of both high Q factor and small dimensions are difficult to realize, because these attributes are mutually contradictory: to have large FSR, a small circumference and bending radius are required. Under such conditions, the efficiency of the TIR confinement mechanism is significantly reduced, leading to larger power radiation and lower Q factors due to bending losses [12].

Photonic crystal (PC) cavities have been extensively studied for high-Q cavity applications. PC cavities with Q factors approaching $\sim 10^6$ were predicted numerically [13], and Qs of up to 4.5×10^4 were demonstrated experimentally [14]. Nevertheless, these resonators consist primarily of a defect (either point or line), which does not necessarily support a whispering gallery mode (WGM)-like solution and are therefore difficult to couple to conventional waveguides. Hexagonal (noncircular) cavities incorporating 120° abrupt bends, which can be easily coupled to PC line defect waveguides, have also been proposed and studied [15]. However, abrupt bends have been shown to support localized bound states [11] which might lase in addition to the desired WGM.

Recently, we proposed utilizing Bragg reflection instead of TIR as the radial confinement mechanism [16]. This concept is illustrated in Fig. 1. A circumferentially guiding defect is located within a medium which consists of annular Bragg layers. Resonators of this class, known as annular Bragg resonators (ABR), are designed to support azimuthally propagating modes, with energy concentrated within the defect region by radial Bragg reflection. Unlike conventional resonators, the reflectivity of the Bragg mirrors can be increased simply by adding more layers. As a result, the radius of the defect, and therefore the modal volume, can be reduced significantly without increasing the bending losses.

Disk and ring resonators based on distributed Bragg reflection have been analyzed previously for both laser and passive resonator applications, employing various techniques such as conformal mapping, a coupled-mode approach and field transfer matrices [17]–[24].

In this paper, we explore theoretically and experimentally the properties of ABRs. In Section II, we briefly review the theoretical framework and the rules for the design and analysis of the resonators. In Section III, we study the advantages of the ABR structure for various applications, and in Section IV, we detail the fabrication of ABRs in semiconductor materials. In Section V, we present experimental results on ABR lasers, discussing our results in Section VI.

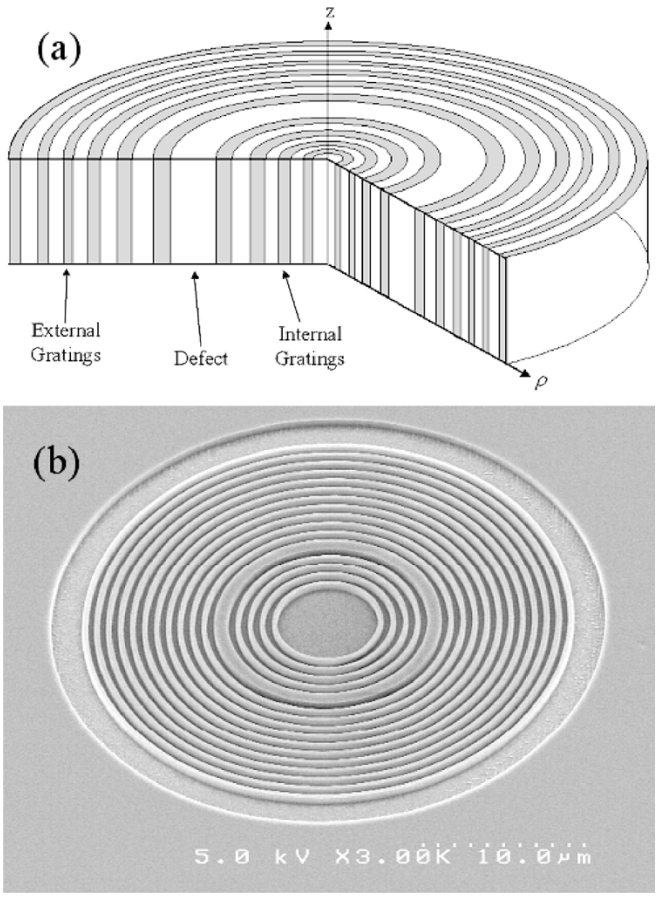

Fig. 1. (a) Schematic of an ABR. (b) Scanning electron microscope (SEM) image of an ABR realized in InGaAsP.

II. Design and Analysis

A. Theoretical Framework

We consider an azimuthally symmetric structure as illustrated in Fig. 1. The guiding defect, which consists of a material with refractive index $n_{\rm def}$, is surrounded by distributed Bragg reflectors on both sides where the reflector layers are of refractive indexes n_1 and n_2. All the electromagnetic field components can be expressed by the z components of the electrical and magnetic fields [25], which satisfy the Helmholtz equation

$$\left[\frac{1}{\rho}\frac{\partial}{\partial\rho}\left(\rho\frac{\partial}{\partial\rho}\right)+\frac{1}{\rho^2}\frac{\partial^2}{\partial\theta^2}+k_0^2n^2(\rho)+\frac{\partial^2}{\partial z^2}\right]\begin{pmatrix}E_z\\H_z\end{pmatrix}=0 \tag{1}$$

where ρ, z and θ are the radial, axial, and azimuthal coordinates, respectively, and k_0 is the wavenumber in vacuum. The refractive index $n(\rho)$ equals either n_1, n_2, or $n_{\rm def}$ depending on the radius ρ. Assuming the dependence of the fields on the coordinates can be separated, the radial part of the fields (either H_z or E_z), $R_{H,E}$, must satisfy the Bessel equation

$$\rho^2\frac{\partial^2R_{H,E}}{\partial\rho^2}+\rho\frac{\partial R_{H,E}}{\partial\rho}+\left[\left(k^2(\rho)-\beta^2\right)\rho^2-m^2\right]R_{H,E}=0 \tag{2}$$

where $k(\rho)=k_0{\cdot}n(\rho)$, m is an integer and β is the z component of the wave vector. The solutions of (2) are a superposition of the mth-order Bessel functions of the first and second kind

$$\begin{aligned}E_z&=\left[A\cdot J_m\left(\sqrt{k_j^2-\beta^2}\rho\right)+B\cdot Y_m\left(\sqrt{k_j^2-\beta^2}\rho\right)\right]\\&\quad\times\cos(\beta\cdot z+\varphi)\cdot\exp(im\theta)\\H_z&=\left[C\cdot J_m\left(\sqrt{k_j^2-\beta^2}\rho\right)+D\cdot Y_m\left(\sqrt{k_j^2-\beta^2}\rho\right)\right]\\&\quad\times\sin(\beta\cdot z+\varphi)\cdot\exp(im\theta)\end{aligned} \tag{3}$$

where A, B, C, and D are independent coefficients and k_j is the material wavenumber in the jth layer. The other four components of the electric and magnetic fields can be readily derived from (3).

The parallel component of the fields—E_z, H_z, E_θ, and H_θ—must be continuous at the interfaces separating successive layers. This requirement can be written in from of a transfer matrix, connecting the amplitude vector $[A\ B\ C\ D]$ in the jth and $j+1$ layers

$$\begin{pmatrix}A_{j+1}\\B_{j+1}\\C_{j+1}\\D_{j+1}\end{pmatrix}=\tilde{M}_{j+1}^{-1}(\rho_{j+1})\cdot\tilde{M}_j(\rho_j)\cdot\begin{pmatrix}A_j\\B_j\\C_j\\D_j\end{pmatrix} \tag{4}$$

and $\tilde{M}_j$ is given by (5) (see bottom of page) where ε and μ are the dielectric and magnetic susceptibilities, ω is the optical angular frequency, $\gamma_j=\sqrt{k_j^2-\beta^2}$, and the primes indicate derivative with respect to the function argument.

In the limit of strong vertical confinement (i.e., $\beta\ll k_j$) it is possible to separate the modal field solutions into two distinct polarizations: TE, consisting of H_z, E_ρ, and E_θ, and TM, consisting of E_z, H_ρ, and H_θ. Unlike [16], we adopt the polarization convention of planar optics.

In the above-mentioned limit, each polarization component can be described by two coefficients in each layer: A_j and B_j for TM and C_j and D_j for TE. For each polarization, the boundary conditions at the interfaces between successive layers can be represented similarly to (4) using simplified 2×2 matrices

$$\begin{aligned}\tilde{M}_j^{\rm TM}&=\begin{pmatrix}J(\gamma_j\rho)&Y(\gamma_j\rho)\\\frac{n_j^2}{\gamma_j}J'(\gamma_j\rho)&\frac{n_j^2}{\gamma_j}Y'(\gamma_j\rho)\end{pmatrix}\\\tilde{M}_j^{\rm TE}&=\begin{pmatrix}J(\gamma_j\rho)&Y(\gamma_j\rho)\\\frac{1}{\gamma_j}J'(\gamma_j\rho)&\frac{1}{\gamma_j}Y'(\gamma_j\rho)\end{pmatrix}.\end{aligned} \tag{6}$$

$$\tilde{M}_j=\begin{pmatrix}J(\gamma_j\rho)&Y(\gamma_j\rho)&0&0\\\frac{n_j^2}{\gamma_j}J'(\gamma_j\rho)&\frac{n_j^2}{\gamma_j}Y'(\gamma_j\rho)&\frac{m\beta}{\rho\omega\varepsilon_0\gamma_j^2}J(\gamma_j\rho)&\frac{m\beta}{\rho\omega\varepsilon_0\gamma_j^2}Y(\gamma_j\rho)\\0&0&J(\gamma_j\rho)&Y(\gamma_j\rho)\\\frac{m\beta}{\rho\omega\mu\gamma_j^2}J(\gamma_j\rho)&\frac{m\beta}{\rho\omega\mu\gamma_j^2}Y(\gamma_j\rho)&\frac{1}{\gamma_j}J'(\gamma_j\rho)&\frac{1}{\gamma_j}Y'(\gamma_j\rho)\end{pmatrix} \tag{5}$$

Using (4) and the matrices (6), the field components can be "propagated" from the inner layers to the external layers. We use the finiteness of the field at $\rho = 0$ so that $B_1 = D_1 = 0$. The second boundary condition is no inward propagating field beyond the last layer, so that $B_{N+1} = -iA_{N+1}$ for TM and $C_{N+1} = -iD_{N+1}$ for TE, where N is the number of layers.

B. Design Rules

The transfer matrix formalism enables us to find the modal field distribution in the case of an arbitrary arrangement of annular concentric dielectric rings. However, we are especially interested in structures that can lead to a concentration of the modal energy near a predetermined radial distance, i.e., within the defect.

It has been shown that the best strategy to attain an exponential decrease (or increase) in the field intensity in the grating region is to position the interfaces of the layers at the zeros and extrema of the z component of the field [26]. The index profile and the field are calculated simultaneously, using the index to find the field and the field to determine the position of the interfaces.

It should be noted that the resulting optimal index profile exhibits an inherent resemblance to the conventional (Cartesian) Bragg reflector. The optimal Cartesian Bragg reflector can be designed in a similar way, leading to layers that are quarter-wavelength thick [27]. Here the resulting layers are also "quarter-wavelength" thick but in the sense of the quasi-periodicity of the mth-order Bessel function [28]. The defect (again, as in the Cartesian case) should be "half-wavelength" wide, i.e., its interfaces should be located at successive zeros of the field.

In order to attain a transverse field profile which is confined within the defect, the profile must exponentially increase for $\rho < \rho_{\text{def}}$ and exponentially decrease for $\rho > \rho_{\text{def}}$. This requirement determines which index interfaces (low $\rightarrow$ high or high $\rightarrow$ low) should be positioned at zeros of the field and which at the extrema of the field. The constraints on the index profile are similar to the Cartesian case and differ for the TE and TM polarizations [26]. For the TE polarization, the interfaces for decreasing (increasing) field should be at the zeros (extrema) of H_z if $n(\rho^-) > n(\rho^+)$ at the interface and at the extrema (zeros) of H_z if $n(\rho^-) < n(\rho^+)$ at the interface. For the TM polarization, the interfaces for decreasing (increasing) field should be at the extrema (zeros) of E_z if $n(\rho^-) > n(\rho^+)$ at the interface and at the zeros (extrema) of E_z if $n(\rho^-) < n(\rho^+)$ at the interface. The interfaces of the defect must be located at zeros of H_z for TE and of E_z for TM.

C. Mode Profile

Fig. 2 depicts the refractive index [Fig. 2(a)] and the TE modal field [Fig. 2(b)] profiles of an ABR designed for a 0.55-μm-thick InGaAsP layer suspended in air. The device is designed to have a mode with an angular propagation coefficient of $m = 7$ at $\lambda_{\text{res}} = 0.852$ μm. The effective index approximation in the vertical dimension is used to reduce the three-dimensional (3-D) problem to a two-dimensional (2-D) equivalent one. As can be seen in the figure, the field is primarily confined in the defect, and it decays while oscillating in the Bragg reflectors.

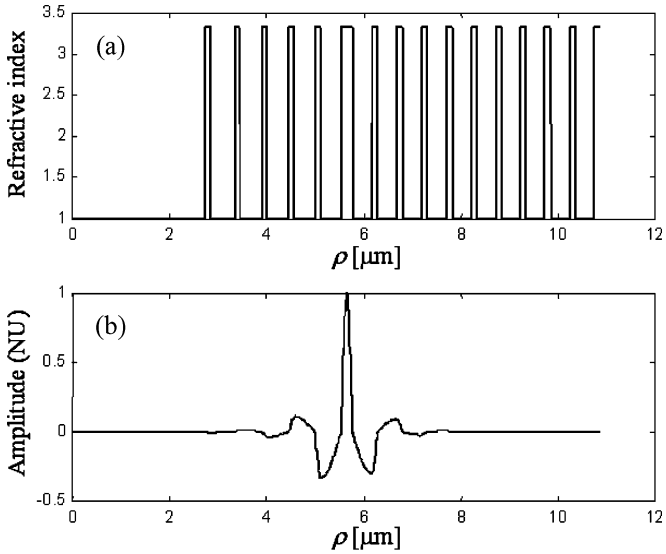

Fig. 2. (a) Refractive index and (b) TE-polarized modal field profiles of an ABR designed for $m = 7, \lambda_{\text{res}} = 0.852\ \mu$m, with five internal and ten external Bragg layers.

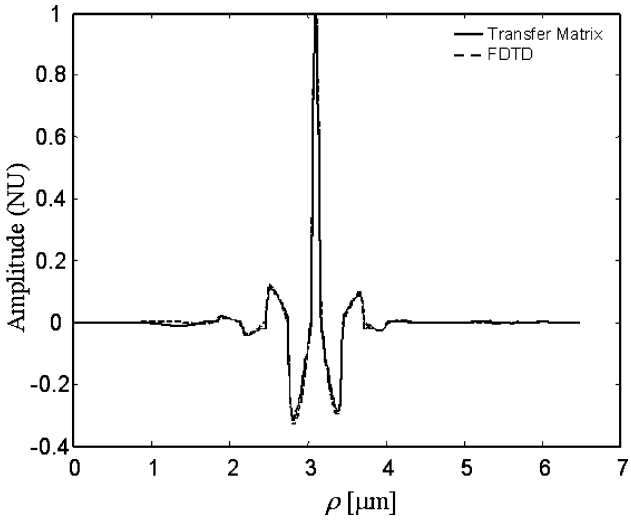

Fig. 3. Comparison between the TE mode profiles calculated by the 2-D transfer matrix approach (solid) and the exact solution obtained by 3-D FDTD (dashed).

To verify the validity of the effective index approximation, we simulate the device using an angular finite-difference-time-domain (FDTD) scheme which takes advantage of the azimuthal symmetry to reduce the computational domain [29]. For a given m, the method can be used to find the resonance wavelength, the quality factor, and the modal field profile of any circular device.

Fig. 3 depicts a comparison between the field profiles calculated by the FDTD simulation and by the 2-D transfer matrix formalism. There is good agreement between the two approaches. The resonance wavelength found by the FDTD simulations is 0.85 μm, and the ratio between H_z and E_z is 25 dB, indicating that the modal field is primarily TE polarized.

Due to the different radial confinement mechanism, the characteristics of the ABR modal field differ significantly from those of the mode of a conventional resonator. First, the radial position of the maximal intensity of the field can be predetermined regardless of wavelength and material system. Second, low angular propagation coefficients (m) and tight bending radius can

be realized because there is no need to satisfy a TIR condition. Finally, the field can be confined in a *lower* refractive index layer, giving rise to a larger FSR or enhanced sensitivity for sensing application (see Section III).

III. Applications

As mentioned previously, the unique characteristics of the ABR mode profile can be advantageous for various applications such as sensing, cavity QED, and telecommunication.

A. Sensing

Of special interest is the possibility of confining the light in a defect consisting of low refractive index medium (such as air), which can be used to attain strong interaction between the cavity photons and any desired material. This characteristic can be used to realize sensitive and compact sensors, which are able to detect small quantities and low concentrations of analyte.

Among the most straightforward approaches for optoelectronic (bio)chemical sensing is to detect the change in the refractive index or the absorption caused by the presence of a (bio)chemical agent. Several schemes have been suggested to detect these types of changes, employing directional couplers [30], Mach–Zehnder interferometers (MZI) [31], or high-Q optical resonators [7]. The detection mechanism underlying these sensors is the modification of the phase accumulation rate (i.e., the propagation coefficient) of the field due to the interaction of the evanescent tail of the field with the analyte.

The primary disadvantage of these detection methods is that the interaction of the field with the surrounding environment is weak, and therefore the influence of the analyte on the propagation coefficient is small. As a result, achieving high sensitivity requires large interaction length leading to the requirement of long interferometers and very high-Q resonators. In addition, the MZI-type sensors might have difficulties detecting small numbers (or single) molecules, regardless of their length.

On the other hand, the ABR structure and mode profile (see Fig. 2) allow for the interaction of the *nonevanescent* part of the field, especially when the device is designed to include an air defect. As a result, ABR-based sensors are expected to offer significantly enhanced sensitivity compared to sensors that are based on conventional resonators of similar dimensions and materials.

Fig. 4 shows a comparison between the shifts of the resonance frequency of an ABR and a conventional ring resonator due to changes in the refractive index of the surroundings. The ABR consists of alternating layers with refractive indexes of 1.545 and 1.0 and an air defect. The conventional resonator consists of $n = 1.545$ core surrounded by air cladding. Both resonators are approximately 16 μm in diameter and designed to resonate in the visible wavelength regime. The sensitivity of each device is indicated by the slope of the curves shown in Fig. 4. The resonance wavelength of the conventional ring resonator shifts by approximately 0.007 nm for an increase of 10^{-3} in the refractive index. For the same index change, the Bragg resonator's resonance wavelength shifts by 0.4 nm, i.e., the ABR exhibits higher sensitivity by a factor of 60.

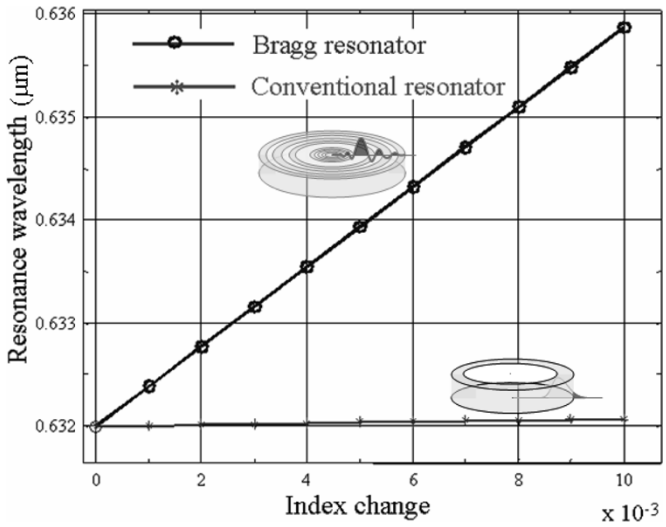

Fig. 4. Comparison of the calculated sensitivity of an ABR and a conventional ring resonator to changes in the refractive index of the surroundings.

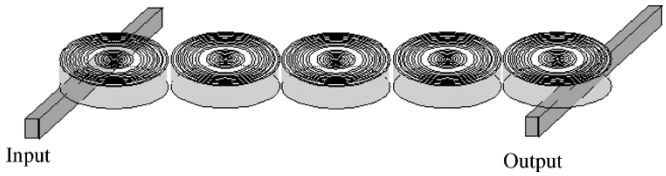

Fig. 5. Illustration of ABR-based CROW employing a vertical coupling scheme to conventional waveguides.

B. Telecommunication

Properties such as large FSR and high Q are essential for any resonator-based telecom application, especially filters, add/drop multiplexers, and optical delay lines [1]–[6], as well as for low-threshold lasers.

One of the interesting differences between ABRs and conventional resonators is the in-plane coupling mechanism to other devices. While in a conventional resonator the coupling is evanescent, the coupling between ABRs is direct (i.e., radiative)—similar to the coupling between PC waveguides and defect cavities [32]–[35]. The radiative coupling mechanism has some advantages and drawbacks compared to evanescent coupling. The main advantage is that the coupling can be determined precisely according to the number of Bragg reflection layers. The drawback is that the resonator cannot be directly coupled to an *in-plane* conventional waveguide (i.e., TIR based), but only to a waveguide also possessing a suitably designed periodic structure, such as a transverse Bragg resonance waveguide [36].

Nevertheless, direct coupling to a conventional waveguide is possible by employing a vertical coupling scheme. Moreover, direct in-plane coupling to other ABRs is possible, thus allowing for structures comprising Bragg-reflection based elements in one layer and conventional I/O waveguides in another (see Fig. 5). Such a configuration is useful for the realization of devices that require precise coupling such as coupled-resonator-optical-waveguide (CROW) delay lines and lasers [36], [37].

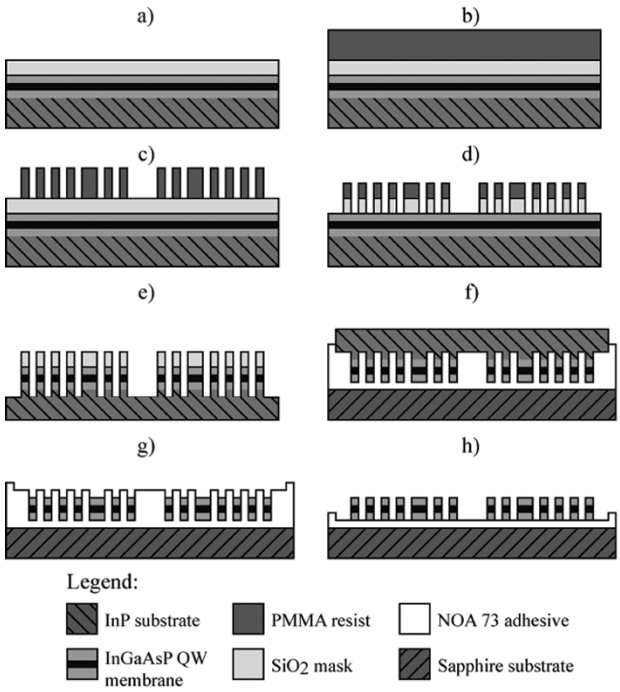

Fig. 6. Fabrication flow diagram and polymer bonding process. The dark regions in the middle of the InGaAsP membrane indicate the QWs. (a) Deposit SiO_2 mask. (b) Spin-coat PMMA e-beam resist. (c) E-beam lithography and develop. (d) SiO_2 ICP etch. (e) Strip PMMA mask and InGaAsP/InP ICP etch. (f) Strip SiO_2 mask and flip bound to sapphire. (g) InGaAsP membrane release. (h) Adhesive ICP etch.

IV. Fabrication

To examine the spectral and spatial properties of the optical modes supported by the ABR structure, we employed high-index-contrast radial Bragg gratings fabricated in active semiconductor material. The semiconductor medium consists of a 250-nm-thick InGaAsP layer ($n \approx 3.35$ at $\lambda = 1.55\ \mu$m) on top of an InP substrate. The InGaAsP layer includes six 75 Å wide compressively strained InGaAsP quantum wells positioned at the center, with peak photoluminescence occurring at 1559 nm.

The fabrication process is illustrated in Fig. 6. First, a SiO_2 etch mask layer is deposited by plasma-enhanced chemical vapor deposition (PECVD) [Fig. 6(a)]. Then, a layer of polymethylmethacrylate (PMMA) electron beam resist is applied by spin-coating [Fig. 6(b)]. The desired geometry is then defined using a direct electron beam writer operating at 100 kV [Fig. 6(c)]. After the resist is developed, the PMMA patterns are transferred into the SiO_2 etch mask layer by inductively coupled plasma reactive ion etching (ICP-RIE) using C_4F_8 plasma [Fig. 6(d)]. The remaining PMMA is removed with a gentle isotropic O_2 plasma step. The SiO_2 layer serves as a hard mask for pattern transfer into the active InGaAsP layer, using an ICP-RIE etch employing HI/Ar chemistry [39] [Fig. 6(e)]. The patterns are etched to a depth of ~325 nm, completely penetrating the active membrane. The remaining SiO_2 hard mask is then stripped in a buffered hydrofluoric acid solution.

To achieve strong vertical confinement, the InGaAsP membrane must be clad by low-index material both above and below. An epitaxial layer transfer technique [40], using a UV-curable optical adhesive, is used to flip-bond the patterned semiconductor sample to a transparent sapphire substrate [Fig. 6(f)]. Subsequently, the InP substrate is removed by mechanical polishing and selective wet chemical etching, leaving the 250-nm-thick patterned InGaAsP membrane embedded in the cured adhesive [Fig. 6(g)]. Finally, the adhesive filling the trenches is removed with an isotropic NF_3/O_2 ICP-RIE etch [Fig. 6(h)]. Fig. 7 depicts SEM images of an ABR device at various stages of the fabrication.

Since the optical emission and gain from the compressively strained quantum wells favor TE-polarized electric fields [41], the design of the fabricated devices is optimized for this polarization. In order to simplify the design calculations, we employ the effective index approximation in the vertical dimension. An effective index $n_{\text{eff}} = 2.8$ is found by solving for the TE-polarized mode of the transferred InGaAsP slab. To facilitate the fabrication of the device, a mixed Bragg order scheme is used, with second-order $(3\lambda/4 \sim 430\ \text{nm})$ high-index layers and first-order $(\lambda/4 \sim 400\ \text{nm})$ low-index layers.

In addition to relaxing the fabrication tolerances, the mixed Bragg order implementation induces a coherent diffraction component in the vertical direction [15]. Although this mechanism reduces the overall Q of the cavity, it facilitates the observation and measurement of the resonator emission.

V. Experiments

The near-field (NF) intensity pattern and the emitted spectrum of the ABRs are examined at room temperature under pulsed optical pumping. Fig. 8 depicts the experimental setup used to characterize the fabricated devices. The pump beam is focused on the sample with a 50X objective lens. The position of this lens is used to control the size and the position of the pump spot. A 20X objective lens is used to collect the vertical emission from the sample and to focus it on an IR camera to obtain the NF intensity pattern and to couple the light into a multimode fiber to obtain the emitted spectrum.

The resonators are pumped by pulsed optical excitation, using a mode-locked Ti : sapphire laser emitting ~120-fs full-width at half-maximum (FWHM) pulses at a repetition rate of 76.6 MHz, with a center wavelength of $\lambda_p = 890$ nm. The pump beam incidents normal to the plane of the devices under test. When the unpatterned QW layer structure is pumped, the emitted spectrum consists of a wide peak centered at 1559 nm. As the pumping power is increased from 1 to 20 mW, the FWHM of the luminescence broadens from approximately 70 to 110 nm, and the peak of the photoluminescence shifts toward longer wavelength due to heating. No significant shift is observed when the pump power is below 5 mW, indicating that heating is of less significance at these pump levels.

When an ABR is pumped, the emission characteristics change significantly. While the specific details (threshold levels, emitted wavelengths, etc.) vary from device to device, the overall behavior is similar. Once a certain pump intensity threshold is exceeded, clear and narrow (~0.5 nm FWHM) emission lines appear in the spectrum (see Fig. 9). As the pump intensity is increased, the intensity of the emission lines increase as well, and they broaden toward shorter wavelengths.

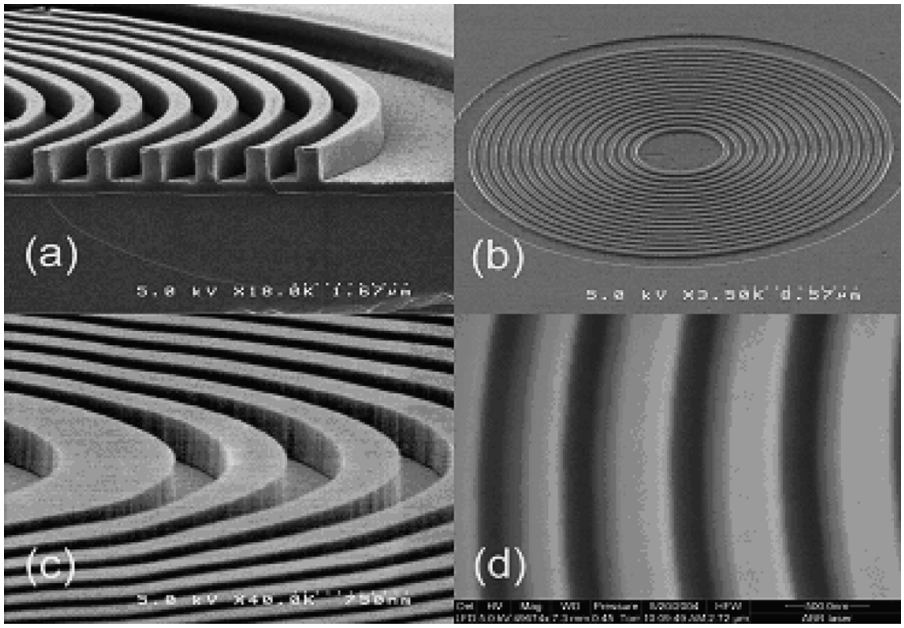

Fig. 7. SEM images of an ABR in various stages of the fabrication process. (a) Cross section of PMMA pattern after electron beam lithography and development. The SiO_2 mask layer can be seen between the PMMA and the substrate. (b) Image taken after the SiO_2 mask removal. The radial defect is the sixth ring from the center. (c) Magnified image of etched semiconductor grating, illustrating vertical and smooth sidewalls. (d) Magnified ESEM image of semiconductor rings, taken after the membrane was transferred to the sapphire substrate and the optical adhesive was etched.

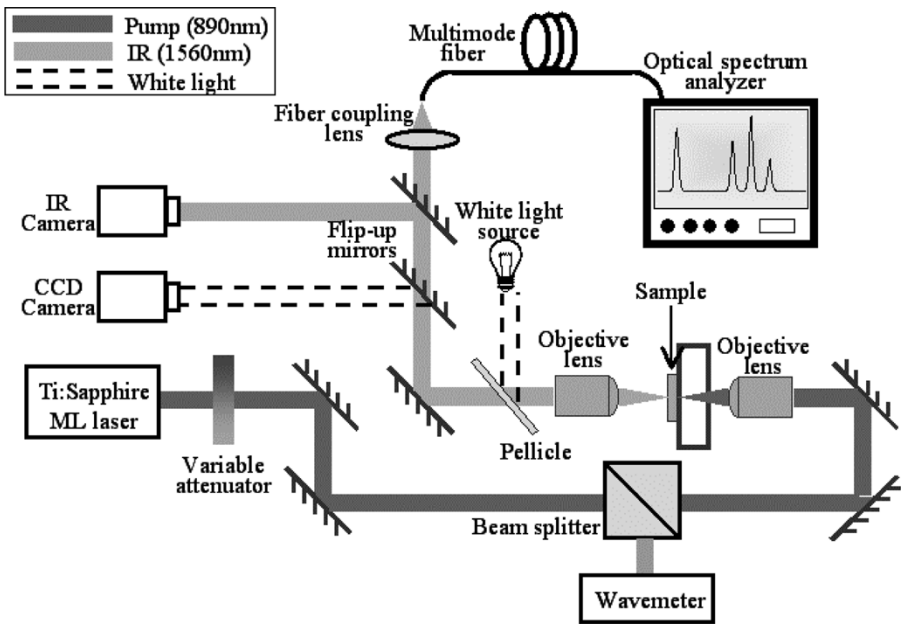

Fig. 8. Schematic of the experimental setup. The dark and the light gray lines indicate the pump and emission beam paths, respectively.

Increasing the pump power further results in the appearance of additional emission lines.

Fig. 9 shows the lasing characteristics at different pump levels of an ABR consisting of five internal and ten external Bragg layers and a half-wavelength wide defect. The radius of the defect is approximately 5 μm. At low pump levels, below 0.75 mW, only a single emission line at 1.595 μm is visible (the device was design to have a resonance wavelength at 1.6 μm). As the pump level is increased, additional resonances at both lower and shorter wavelength appear although the peak at 1.595 μm remains the dominant one. The inset of Fig. 9 depicts the integrated emitted power from the lasers versus the pump level, indicating a clear lasing threshold at $P_{\text{pump}} = 680\,\mu\text{W}$. Although the laser was designed for a specific mode, Fig. 9 indicates the existence of additional lasing modes. The existence of these modes stem from the combination of the large index contrast between the Bragg layers, which generated an effective radial "bandgap," and the use of three-quarter-wavelength layers consisting of high-index material, which effectively elongate the defect circumference. As a result, the device also supports additional radial and azimuthal modes. However, because the radial index profile is optimized to a specific modal

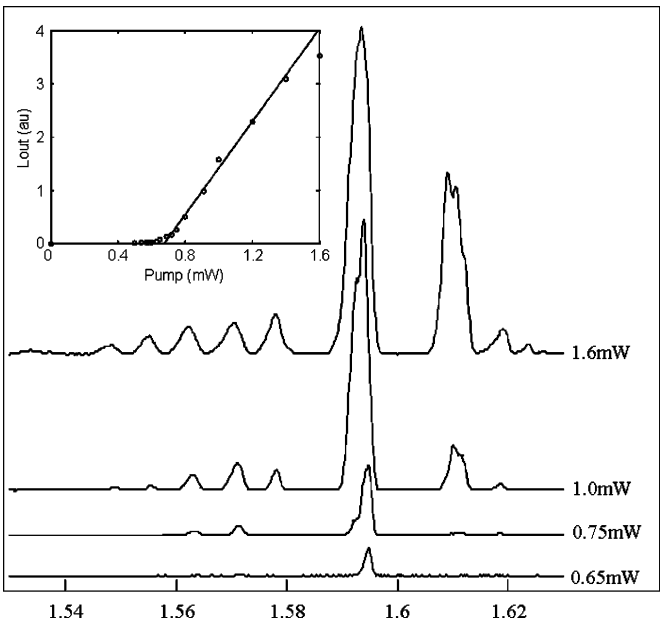

Fig. 9. Optical spectra emitted from a lasing ABR under different pump levels. Spectra are vertically offset to illustrate the effects of increasing pump power. Inset: integrated emitted power versus pump power, showing laser threshold at $\sim$ 680 μWP.

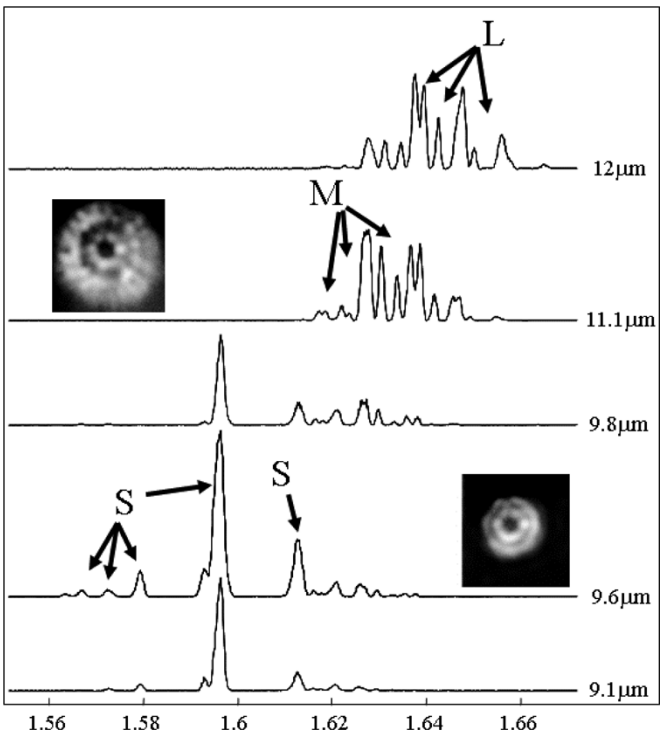

Fig. 10. Measured spectra for various pump-spot diameters. The labels "S," "M," and "L" indicate modes located at short, medium, and large radii, respectively. Insets: IR image of the emitted pattern at the 9.6- and 11.1-μm-wide pump.

field profile, these additional modes are lossier, and thus their threshold pump levels are higher.

We also studied the impact of the pump-spot dimensions on the emission characteristics. By changing the size of the pumped area it is possible to selectively excite the resonant modes of the cavity according to their radial profile. Fig. 10 shows measured spectra from the same device as that of Fig. 9, for increasing pump-spot diameters. The pump level is maintained constant at 1.2 mW. Thus, as the pump spot is increased, the pump density decreases at the center of the device and increases in the periphery, effectively scanning over the resonator area. As the pump spot is broadened, spectral features having longer wavelength and smaller FSR appear, with the most prominent transition occurring between 10- and 11-μm diameter pump spots.

We assume that resonances that appear at larger pump spots peak at larger radii within the device. Under this assumption, the resonance frequencies of the device can be categorized into three distinct groups according to their radial profile. These groups, marked as "S", "M," and "L," are located at small, medium, and large radii, respectively (see Fig. 10). The insets of Fig. 10 show the IR emission pattern from the ABR at pump-spot diameters of 9.6 and 11.1 μm. The emitted pattern at $\mathrm{D_{pump}} = 9.6$ μm consists of two bright rings: an inner ring with an angular propagation coefficient of $m = 3$ and an outer ring whose angular propagation coefficient cannot be resolved. The outer ring is located at the radial defect of the device. We attribute these modes to the strongest peaks in the corresponding spectrum at $\lambda = 1595$ nm and at $\lambda = 1615$ nm. The pattern at $\mathrm{D_{pump}} = 11.1$ μm includes the inner ring with $m = 3$ but does not exhibit the outer ring observed for the smaller pump spot. Since wider pump spots are associated with longer wavelength, we infer that the inner ring corresponds to $\lambda = 1615$ nm and that the defect mode corresponds to $\lambda = 1595$ nm. As can be expected, the pattern at $\mathrm{D_{pump}} = 11.1$ μm is wider than the one at $\mathrm{D_{pump}} = 9.6$ μm and exhibits modes which are located at larger radii.

VI. Discussion and Conclusion

We have studied, experimentally and theoretically, the characteristics of a novel class of lasers that are based on radial Bragg reflectors. Lasing action with low threshold levels are demonstrated at room temperature under pulsed optical pumping. The observed Q factors are between 1000 and 2000.

By changing the pump-spot diameter, we find that longer resonance wavelengths correspond to patterns with larger radii for the specific structure presented here. For this device, it is possible to correlate between some of the resonance wavelengths and the observed IR patterns, and to identify one of the defect modes.

Such laser sources are ideally suited to the detection of small changes in the modal effective index or the Q factor and for achieving strong atom-field coupling. In addition, our cavity can easily be integrated with other photonic devices such as photonic crystals and distributed feedback lasers.

Acknowledgment

The authors would like to thank Dr. A. Scherer and Dr. O. Painter for providing access to their fabrication facilities. Fruitful discussions with J. Poon and G. Paloczi are also acknowledged.

REFERENCES

[1] C. K. Madsen and J. H. Zhao, *Optical Filter Design and Analysis: A Signal Processing Approach*. New York: Wiley-Interscience, 1999.

[2] B. E. Little, "Ultracompact Si–SiO2 microring resonator optical dropping filter," *Opt. Lett.*, vol. 23, pp. 1570–1572, Oct. 1998.

[3] A. Melloni, R. Costa, P. Monguzzi, and M. Martinelli, "Ring-resonator filters in silicon oxynitride technology for dense wavelength-division multiplexing systems," *Opt. Lett.*, vol. 28, pp. 1567–1569, Sep. 2003.

[4] A. Yariv, "Critical coupling and its control in optical waveguide-ring resonator systems," *IEEE Photon. Technol. Lett.*, vol. 14, no. 4, pp. 483–485, Apr. 2002.

[5] J. E. Heebner and R. W. Boyd, "'Slow' and 'fast' light in resonator-coupled waveguides," *J. Mod. Opt.*, vol. 49, pp. 2629–2636, Dec. 2002.

[6] A. Melloni, F. Morichetti, and M. Martinelli, "Linear and nonlinear pulse propagation in coupled resonator slow-wave optical structures," *Opt. Quantum Electron.*, vol. 35, pp. 365–379, Apr. 2003.

[7] R. E. Boyd and J. Heebner, "Sensitive disk resonator photonic biosensor," *Appl. Opt.*, vol. 40, pp. 5742–5747, Nov. 2001.

[8] C. Y. Chao and L. J. Guo, "Biochemical sensors based on polymer microrings with sharp asymmetrical resonance," *Appl. Phys. Lett.*, vol. 83, pp. 1527–1529, Aug. 2003.

[9] A. B. Matsko, L. Maleki, A. A. Savchenkov, and V. S. Ilchenko, "Whispering gallery mode based optoelectronic microwave oscillator," *J. Mod. Opt.*, vol. 50, pp. 2523–2542, Nov. 2003.

[10] K. J. Vahala, "Optical microcavities," *Nature*, vol. 424, pp. 839–846, Aug. 2003.

[11] J. Vučković, M. Lončar, H. Mabuchi, and A. Scherer, "Design of photonic crystal microcavities for cavity QED," *Phys. Rev. E*, vol. 65, p. 016 608, Dec. 2001.

[12] E. A. J. Marcatili, "Bends in optical dielectric guides," *AT&T Tech. J.*, vol. 48, pp. 2103–2132, Sep. 1969.

[13] H. Y. Ryu, M. Notomi, G. H. Kim, and Y. H. Lee, "High quality-factor whispering-gallery mode in the photonic crystal hexagonal disk cavity," *Opt. Express*, vol. 12, pp. 1708–1719, Apr. 2004.

[14] Y. Akahane, T. Asano, B. S. Song, and S. Noda, "High-Q photonic nanocavity in a two-dimensional photonic crystal," *Nature*, vol. 425, pp. 944–947, Oct. 2003.

[15] S. Kim, H. Ryu, H. Park, G. Kim, Y. Choi, Y. Lee, and J. Kim, "Two-dimensional photonic crystal hexagonal waveguide ring laser," *Appl. Phys. Lett.*, vol. 81, pp. 2499–2501, Sep. 2002.

[16] J. Scheuer and A. Yariv, "Annular Bragg defect mode resonators," *J. Opt. Soc. Amer. B.*, vol. 20, pp. 2285–2291, Nov. 2003.

[17] M. Toda, "Single-mode behavior of a circular grating for potential disk-shaped DFB lasers," *IEEE J. Quantum Electron.*, vol. 26, no. 3, pp. 473–481, Mar. 1990.

[18] X. H. Zheng and S. Lacroix, "Mode coupling in circular-cylindrical system and its application to fingerprint resonators," *IEEE J. Lightw. Technol.*, vol. 8, no. 10, pp. 1509–1516, Oct. 1990.

[19] M. A. Kaliteevski, R. A. Abram, V. V. Nikolaev, and G. S. Sokolovski, "Bragg reflectors for cylindrical waves," *J. Mod. Opt.*, vol. 46, pp. 875–890, Apr. 1999.

[20] C. Wu, M. Svilans, M. Fallahi, T. Makino, J. Glinski, C. Maritan, and C. Blaauw, "Optically pumped surface-emitting DFB GaInAsP/InP lasers with circular grating," *Electron. Lett.*, vol. 27, pp. 1819–1821, Sep. 1991.

[21] D. Labilloy, H. Benisty, C. Weisbuch, T. F. Krauss, C. J. M. Smith, R. Hourdré, and U. Oesterle, "High-finesse disk microcavity based on a circular Bragg reflector," *Appl. Phys. Lett.*, vol. 73, pp. 1314–1316, Sep. 1998.

[22] D. Ochoa, R. Hourdré, M. Ilegems, H. Benisty, T. F. Krauss, and C. J. M. Smith, "Diffraction of cylindrical Bragg reflectors surrounding an in-place semiconductor microcavity," *Phys. Rev. B*, vol. 61, pp. 4806–4812, Feb. 2000.

[23] J. Scheuer and A. Yariv, "Two-dimensional optical ring resonators based on radial Bragg resonance," *Opt. Lett.*, vol. 28, pp. 1528–1530, Sep. 2003.

[24] J. Scheuer, W. M. J. Green, G. DeRose, and A. Yariv, "Low threshold two-dimensional annular Bragg lasers," *Opt. Lett.*, vol. 29, pp. 2641–2643, Nov. 2004.

[25] A. Yariv, *Optical Electronics in Modern Communications*, 5th ed. New York: Oxford Univ. Press, 1997.

[26] P. Yeh, A. Yariv, and E. Marom, "Theory of Bragg fiber," *J. Opt. Soc. Amer.*, vol. 68, pp. 1196–1201, Sep. 1978.

[27] A. Yariv and P. Yeh, *Optical Waves in Crystals*. New York: Wiley, 1984.

[28] J. Scheuer and A. Yariv, "Coupled-waves approach to the design and analysis of Bragg and photonic crystal annular resonators," *IEEE J. Quantum Electron.*, vol. 39, no. 12, pp. 1555–1562, Dec. 2003.

[29] S. Shi, L. Yang, and D. W. Prather, "Numerical study of axisymmetric dielectric resonators," *IEEE Trans. Microw. Theory Tech.*, vol. 49, no. 9, pp. 1614–1619, Sep. 2001.

[30] B. J. Luff, R. D. Harris, J. S. Wilkinson, R. Wilson, and D. J. Schiffrin, "Integrated-optical directional coupler biosensor," *Opt. Lett.*, vol. 21, pp. 618–620, Apr. 1996.

[31] B. J. Luff, J. S. Wilkinson, J. Piehler, U. Hollenbach, J. Igenhoff, and N. Fabricius, "Integrated optical Mach–Zehnder biosensor," *IEEE J. Lightw. Technol.*, vol. 16, no. 4, pp. 583–592, Apr. 1998.

[32] M. Koshiba, "Wavelength division multiplexing and demultiplexing with photonic crystal waveguide coupler," *IEEE J. Lightw. Technol.*, vol. 19, no. 12, pp. 1970–1975, Dec. 2001.

[33] A. L. Reynolds, U. Peschel, F. Lederer, P. J. Roberts, T. F. Krauss, and P. J. de Maagt, "Coupled defect in photonic crystals," *IEEE Trans. Microw. Theory Tech.*, vol. 49, no. 10, pp. 1860–1867, Oct. 2001.

[34] T. J. Karle, Y. J. Chai, C. N. Morgan, I. H. White, and T. F. Krauss, "Observation of pulse compression in photonic crystal coupled cavity waveguides," *IEEE J. Lightw. Technol.*, vol. 22, no. 2, pp. 514–519, Feb. 2004.

[35] Z. Wang and S. Fan, "Compact all-pass filters in photonic crystal as the building block for high-capacity optical delay lines," *Phys. Rev. E.*, vol. 68, p. 066 616, Dec. 2003.

[36] A. Yariv, "Coupled-wave formalism for optical waveguiding by transverse Bragg reflection," *Opt. Lett.*, vol. 27, pp. 936–938, Jun. 2002.

[37] A. Yariv, Y. Xu, R. K. Lee, and A. Scherer, "Coupled-resonator optical waveguide: a proposal and analysis," *Opt. Lett.*, vol. 24, pp. 711–713, Jun. 1999.

[38] S. Mookherjea, "Semiconductor coupled-resonator optical waveguide laser," *Appl. Phys. Lett.*, vol. 84, pp. 3265–3267, Apr. 2004.

[39] S. J. Pearton, U. K. Chakrabarti, A. Katz, F. Ren, and T. R. Fullowan, "High-rate, anisotropic dry etching of InP in HI-based discharges," *Appl. Phys. Lett.*, vol. 60, pp. 838–840, Feb. 1992.

[40] S. R. Sakamoto, C. Ozturk, Y. T. Byun, J. Ko, and N. Dagli, "Low-loss substrate-removed (SURE) optical waveguides in GaAs-AlGaAs epitaxial layers embedded in organic polymers," *IEEE Photon. Technol. Lett.*, vol. 10, no. 7, pp. 985–987, Jul. 1998.

[41] L. A. Coldren and S. W. Corzine, *Diode Lasers and Photonic Integrated Circuits*. New York: Wiley-Interscience, 1995.

Jacob Scheuer (S'99–M'01) received the B.Sc. degrees in electrical engineering and in physics (*summa cum laude*) and the Ph.D. degree in electrical engineering from the Technion–Israel Institute of Technology, Haifa, in 1993 and 2001, respectively. His doctoral research involved theoretical and experimental study of the formation of complex light patterns and optical vortices in vertical cavity surface emitting lasers (VCSELs) and the interactions between scalar/vector spatial solitons.

Currently, he is a Postdoctoral Associate in the Department of Applied Physics, California Institute of Technology, Pasadena. His current research interests include annular Bragg and photonic crystal resonators as well as coupled resonators optical waveguides (CROWs).

William M. J. Green (S'03), photograph and biography not available at the time of publication.

Guy A. DeRose received the B.S. degree in physics from Indiana University of Pennsylvania, Indiana, PA, in 1987 and the M.S. and Ph.D. degrees in physics from Case Western Reserve University. Cleveland, OH, in 1989 and 1992, respectively, where he studied thin-film mechanical properties via X-ray absorption spectroscopy.

He has been the Laboratory Coordinator of Prof. A. Scherer's nanofabrication group at California Institute of Technology (Caltech), Pasadena, since 2000, where he studies integration of optics with microfluidics and physical properties and fabrication of nanometer-scale wires. He is also Codirector of Caltech's Large-Scale Integration of Nanostructures Laboratory, in which he is performing research on electron beam lithography.

Amnon Yariv (S'56–M'59–F'70–LF'95), a native of Israel, received the B.S., M.S., and Ph.D. degrees in electrical engineering from the University of California, Berkeley, in 1954, 1956, and 1958, respectively.

In 1959, he went to the Bell Telephone Laboratories, Murray Hill, NJ, joining the early stages of the laser effort. In 1964, he joined the California Institute of Technology, Pasadena, as an Associate Professor of Electrical Engineering, becoming a Professor in 1966. In 1980, he became the Thomas G. Myers Professor of Electrical Engineering and Applied Physics. In 1996, he became the Martin and Eileen Summerfield Professor of Applied Physics and Professor of Electrical Engineering. On the technical and scientific sides, he took part (with various coworkers) in the discovery of a number of early solid-state laser systems, in the original formulation of the theory of nonlinear quantum optics; in proposing and explaining mode-locked ultrashort-pulse lasers and GaAs optoelectronics; in proposing and demonstrating semiconductor-based integrated optics technology; in pioneering the field of phase conjugate optics; and in proposing and demonstrating the semiconductor-distributed feedback laser. His current research efforts are in the areas of nonlinear optics, semiconductor lasers and wavelength-division multiplexing (WDM) filters, especially the problem of monolithic integration of transistors, injection lasers, ultrafast (<1 ps) semiconductor devices and phenomena, and the propagation of optical signals in fibers, including WDM. He has published widely in the laser and optics fields and has written a number of basic texts in quantum electronics, optics, and quantum mechanics.

Dr. Yariv is a Member of the American Physical Society, Phi Beta Kappa, the American Academy of Arts and Sciences, the National Academy of Engineering, and the National Academy of Sciences, and a Fellow of the Optical Society of America. He has received the 1980 Quantum Electronics Award of the IEEE, the 1985 University of Pennsylvania Pender Award, the 1986 Optical Society of America Ives Medal, the 1992 Harvey Prize (shared with M. Gorbachev) and the 1998 Esther Beller Medal of the Optical Society of America. He is a Founder and Chairman of the Board of ORTEL Corporation (acquired by Lucent Technologies) and a Founder and Board Member of Arroyo Optics Inc.